Supporting Information

Lee et al. 10.1073/pnas.1106368108

SI Text

Derivation of Size Distribution for Complete Energy Leads to Problems at $R = 0$. A size distribution can be derived directly from the exact energy expression:

$$\frac{E}{N}-\frac{E}{M}=\mu_N^{\circ}-\mu_M^{\circ}=\frac{2a}{R}\left[\lambda-\frac{(\Delta m)^2}{4\pi\varepsilon\varepsilon_{\rm o}}\ln\left(\frac{4R}{e^2\delta}\right)\right] -\frac{2a}{R_{\rm o}}\left[\lambda-\frac{(\Delta m)^2}{4\pi\varepsilon\varepsilon_{\rm o}}\ln\left(\frac{4R_{\rm o}}{e^2\delta}\right)\right]. \quad [S1]$$

Using the results of Eq. **2** for $R_{\rm o}$ in the final term of Eq. **S1**, this simplifies to

$$\frac{E}{N}-\frac{E}{M}=\left(\frac{2a}{R}\right)\left(\frac{(\Delta m)^2}{4\pi\varepsilon\varepsilon_{\rm o}}\right)\left[\ln\left(\frac{R_{\rm o}}{R}\right)-1+\frac{R}{R_{\rm o}}\right] \quad [S2]$$

and the size distribution becomes

$$C_N=\left\{C_M\exp\left[-2\beta\left[1+\frac{R_{\rm o}}{R}\left(\ln\left(\frac{R_{\rm o}}{R}\right)-1\right)\right]\right]\right\}^{R^2/R_{\rm o}^2} =\left\{C_M\exp\left[-2\beta\left[1-\frac{R_{\rm o}}{R}\left(\ln\left(\frac{R}{R_{\rm o}}\right)+1\right)\right]\right]\right\}^{R^2/R_{\rm o}^2} \quad [S3]$$

with the same parameter, $\beta=\frac{(\Delta m)^2R_{\rm o}}{4\varepsilon\varepsilon_{\rm o}k_{\rm B}T}$. The limit as R goes to 0 is:

$$C_N(R\to 0)=(C_M)^{R^2/R_{\rm o}^2}\exp\left[-2\beta\left(\frac{R^2}{R_{\rm o}^2}\right)\left[1-\frac{R_o}{R}\left(\ln\left(\frac{R}{R_{\rm o}}\right)+1\right)\right]\right] =(C_M)^0\exp(0)=1 \quad [S4]$$

which is not physical, as the probability of any particular domain size must be less than 1. The distribution, as a result, is nonmonotonic for small R; there is a minimum in the distribution and the probability increases to 1 as R goes to zero, which is also not physical.

However, for the quadratic energy distribution, the limit as R goes to zero is given by

$$C_N(R\to 0)=(C_M)^{R^2/R_{\rm o}^2}\exp\left[-\beta\left(\frac{R}{R_{\rm o}}\right)^2\left(\frac{R_{\rm o}}{R}-1\right)^2\right] =(C_M)^0\exp(-\beta)=\exp(-\beta), \quad [S5]$$

which gives a monotonic decrease and more realistic limit as R goes to zero. The quadratic Taylor series expansion in $\rho=1/R$, rather than R, was chosen as it gave a better representation of the full energy for a wider range of R.

In our distributions, we are limited experimentally by the resolution of the fluorescence microscope to $R>0.5$ μm, so the details of the size distribution as R goes to zero are less important, although we expect that a monotonic decrease as R goes to zero is more realistic.

Derivation of Eq. 9. Let us consider the simple 2D geometry (invariant in the plane of the paper) shown in Fig. S1. The thickness of the hydrophobic region of the $L_{\rm d}$ phase is $l_{\rm d}$, while that of the $L_{\rm o}$ phase is $l_{\rm o}$, which is an increase of Δl over $l_{\rm d}$. We assume that the $L_{\rm o}$ and $L_{\rm d}$ regions are bridged by a region in which the $L_{\rm d}$ phase molecules are arranged in a linear profile, as shown in Fig. S1. This linear profile is given mathematically as

$$h(x)=l_{\rm d}+\Delta l\left(1-\frac{x}{L}\right). \quad [S6]$$

Because the $L_{\rm d}$ phase molecules are being stretched to bridge the height difference, the headgroup area a in this region is different from the equilibrium, undistorted value $a_{\rm d}$ in the bulk $L_{\rm d}$ region. If we consider an element of thickness dx, the differential number of molecules in this region per unit length into the plane of the paper, dN, is given by

$$dN=\frac{ds}{a}=\frac{h\,dx}{v}, \quad [S7]$$

where ds is the elemental surface area (Fig. S1), a is the headgroup area at the position x and v are the volume of the hydrophobic region of a single $L_{\rm d}$ phase molecule. Therefore, the headgroup area in the bridging region is distorted to allow the chains to extend at constant volume:

$$\frac{a_{\rm d}}{a}=\frac{a_{\rm d}h(dx/ds)}{v}. \quad [S8]$$

But for the linear profile in Eq. **S6**:

$$\frac{dx}{ds}=\cos\theta, \quad [S9]$$

and so,

$$\frac{a_{\rm d}}{a}=\frac{a_{\rm d}h\cos\theta}{v}. \quad [S10]$$

We take for a model of the line tension the energy per unit length of the distorted region, which is related to the exposed hydrophobic area per unit length (1),

$$\lambda=\gamma\int_0^L\frac{(a_{\rm d}-a)^2}{a}dN=\gamma\int_0^L\frac{(a_{\rm d}-a)^2}{a^2}ds =\gamma\int_0^L\left(\frac{a_{\rm d}}{a}-1\right)^2\frac{ds}{dx}dx=\gamma\int_0^L\left(\frac{a_{\rm d}}{a}-1\right)^2\frac{dx}{\cos\theta} \quad [S11]$$

in which γ is the air-hydrocarbon region interfacial tension. Therefore,

$$\lambda=\gamma\int_0^L\left(\frac{a_{\rm d}h\cos\theta}{v}-1\right)^2\frac{dx}{\cos\theta}. \quad [S12]$$

Substitution of h from Eq. **S6** yields

$$\lambda=\gamma\int_0^L\left(\frac{a_{\rm d}\cos\theta}{v}\left[l_{\rm d}+\Delta l\left(1-\frac{x}{L}\right)-1\right]\right)^2\frac{dx}{\cos\theta}\lambda =\gamma\int_0^L\left(\frac{a_{\rm d}l_{\rm d}\cos\theta}{v}+\frac{a_{\rm d}\Delta l\cos\theta}{v}\left(1-\frac{x}{L}\right)-1\right)^2\frac{dx}{\cos\theta}. \quad [S13]$$

Because $l_d = \nu/a_d$,

$$\begin{aligned}\lambda &= \gamma \int_0^L \left[\cos\theta - 1 + \frac{\Delta l \cos\theta}{l_\mathrm{d}}\left(1 - \frac{x}{L}\right)\right]^2 \frac{\mathrm{d}x}{\cos\theta}\lambda \\ &= \gamma \int_0^L \left[(\cos\theta - 1)^2 + 2(\cos\theta - 1)\frac{\Delta l \cos\theta}{l_\mathrm{d}}\left(1 - \frac{x}{L}\right)\right. \\ &\quad \left. + \left(\frac{\Delta l \cos\theta}{l_\mathrm{d}}\right)^2 \left(1 - \frac{x}{L}\right)^2\right] \frac{\mathrm{d}x}{\cos\theta}\lambda \\ &= \frac{\gamma L}{\cos\theta}\left[(1 - \cos\theta)^2 - (1 - \cos\theta)\frac{\Delta l \cos\theta}{l_\mathrm{d}} + \frac{1}{3}\left(\frac{\Delta l \cos\theta}{l_\mathrm{d}}\right)^2\right]. \end{aligned} \quad \textbf{[S14]}$$

Simplifying this further, we get

$$\lambda = \gamma L\left[\frac{(1 - \cos\theta)^2}{\cos\theta} - (1 - \cos\theta)\frac{\Delta l}{l_\mathrm{d}} + \frac{\cos\theta}{3}\left(\frac{\Delta l}{l_\mathrm{d}}\right)^2\right], \quad \textbf{[S15]}$$

and because $L = \Delta l/\tan\theta$,

$$\lambda = \gamma \Delta l\left[\frac{(1 - \cos\theta)^2}{\sin\theta} - \frac{(1 - \cos\theta)\cos\theta}{\sin\theta}\frac{\Delta l}{l_\mathrm{d}} + \frac{\cos^2\theta}{3\sin\theta}\left(\frac{\Delta l}{l_\mathrm{d}}\right)^2\right]. \quad \textbf{[S16]}$$

When θ is equal to $\pi/2$, there is a step change in height between the two phases, and the line tension is simply the interfacial tension times the change in height, i.e., $\lambda = \gamma\Delta l$, as expected. As θ decreases from $\pi/2$, the height changes more gradually. The stretching of L_d phase molecules in the bridging region decreases, and the line tension falls. However, when θ decreases beyond a critical value θ_crit, the line tension increases because any further decrease in θ only increases the length L of the bridging region and the number of molecules in it, but does not significantly affect the stretching of the molecules. The minimum line tension occurs at $\theta_\mathrm{crit} \approx 180(\Delta l/l_\mathrm{d})^{1/2}/\pi$, at which point $\lambda_\mathrm{min} \approx \{0.08(\Delta l/l_\mathrm{d})^{3/2}\}\gamma\Delta l$.

Table S1 shows line tension calculated for representative values of l_d and Δl. Allowing the interface to transition smoothly between phases gives line tensions of order fN, while a step change gives line tensions of order pN.

A similar model for line tensions based on a smoothed transition between phases is given by Kuzmin et al. (2). Safran and coworkers (3, 4) also have examined smoothing the transition by allowing "line-actant" molecules to preferentially locate at the boundary between domains. In Safran's models, line-actants are molecules that are intermediate in properties between those in the two phases. In the type of system studied here such a situation could arise with molecule having hydrophobic lengths intermediate between the L_o and L_d phases.

SI Materials. The compositions of the lipids in myelin membranes were identified from our previous work by using high performance liquid chromatography (HPLC) and nuclear magnetic resonance (NMR) techniques (5). From the measured total lipid compositions, approximate compositions for the cytoplasmic (CYT) and extracellular (EXT) monolayers were formulated using literature values of the distribution of lipid species (6, 7). In this paper, the following five brain-derived lipids were used to mimic the CYT face of the myelin membrane and to obtain pressure-area (Π-A) isotherms: Phosphatidylserine$^-$ (Porcine brain PS$^-$), sphingomyelin (Porcine brain SM), phosphatidylcholine (Porcine brain PC), phosphatidylethanolamine (Porcine brain PE), and cholesterol (ovine wool) (Avanti Polar Lipids, Alabaster, AL, purity >99%). The major fatty acid chain lengths of the three major lipids (PC, PE, and PS$^-$) are 16:0, 18:0, 18:1 and 20:4. All lipids were stored in chloroform until used. Sodium nitrate, calcium nitrate, and morpholinepropanesulfonic acid (Mops) sodium salt were purchased from Sigma-Aldrich (St. Louis, MO). Texas Red® 1,2-dihexadecanoyl-sn-glycero-3-phophoethanolamine and triethylammonium salt (TR-DHPE) was purchased from Invitrogen (Carlsbad, CA).

SI Methods. The lipid mixtures for control CYT and EAE CYT were dissolved in a solution of hexane:chloroform:ethanol = 11:5:4 (vol/vol) at a total lipid concentration of 1 mg/mL. 12 μL of the 1 mg/mL solution was added drop wise onto a subphase made up of pH 7.2 MOPS [3-(N-morpholino)propanesulfonic acid] buffer (150 mN sodium nitrate / 10 mM Mops sodium salt / 2 mM calcium nitrate) in a custom-built Langmuir trough (8, 9), and the solvent was allowed to evaporate for 5 min. The subphase water was purified with a Millipore Gradient System (Billericca, MA) and had a resistivity of 18.2 MΩ/cm. Isotherms were measured on compression at 22 ± 0.1 °C (See Fig. S2). The surface pressure was monitored during compression using a filter paper Wilhelmy plate. The trough had a surface area of 112 cm^2 with a subphase volume of 150 mL, and a typical compression took 13 min. For fluorescence imaging, 1 wt% TR-DHPE was used to provide contrast in the images, and a Nikon Optiphot optical microscope (Nikon, Tokyo, Japan) with a 40× power long working distance objective coupled to a silicon intensified target (SIT) camera (DAGE-MTI, Sunnyvale, CA), which was positioned above the trough and used for imaging. Full length movies were recorded by a JVC super VHS VCR (Elmwood Park, NJ) and directly imported to a computer (Moviestar, Mountain View, CA). Adobe After Effects CS3 was used for frame capture from the video. Five cells (430 × 300 pixels each) were randomly cropped from captured images (1,152× 774 pixels each) with Adobe Photoshop CS2, followed by analysis with the ImageJ (NIH) program. The domain areas were converted into square microns using a conversion factor (9.38 pixel/μm^2). Domains smaller than 3 × 3 pixels (<0.5 μm radius) were discarded due to the limited resolution. Domain radii were graphically displayed as histograms, with bin numbers equal to the square root of total number of domains. These histograms were fitted with Eq. **8**, using user defined fitting in OriginPro 8 software (see Figs. 2 and 3).

1. Israelachvili JN, Mitchell DJ, Ninham BW (1976) Theory of self-assembly of hydrocarbon amphiphiles into micelles and bilayers. *Journal of the Chemical Society-Faraday Transactions II* 72:1525–1568.
2. Kuzmin PI, Akhimov SA, Chizmadzhev YA, Zimmerberg J, Cohen FS (2005) Line tension and interaction energies of membrane rafts calculated from lipid splay and tilt. *Biophys J* 88:1120–1133.
3. Brewster R, Pincus P, Safran SA (2009) Hybrid lipids as a biological surface-active component. *Biophys J* 97:1087–1094.
4. Brewster R, Safran SA (2010) Line active hybrid lipids determine domain size in phase separation of saturated and unsaturated lipids. *Biophys J* 98:L21–L23.
5. Ohler B, et al. (2004) Role of lipid interactions in autoimmune demyelination. *Biochim Biophys Acta* 1688:10–17.
6. Inouye H, Kirschner DA (1988) Membrane interactions in nerve myelin. *Biophys J* 53:235–245;247–260.
7. Inouye H, Kirschner DA (1988) Membrane interactions in nerve myelin .2. Determination of surface-charge from biochemical data. *Biophys J* 53:247–260.
8. Lee KYC, et al. (1998) Apparatus for the continuous monitoring of surface morphology via fluorescence microscopy during monolayer transfer to substrates. *Langmuir* 14:2567–2572.
9. Lee KYC, Lipp MM, Zasadzinski JA, Waring AJ (1998) Direct observation of phase and morphology changes induced by lung surfactant protein SP-B in lipid monolayers via fluorescence, polarized fluorescence, Brewster angle and atomic force microscopies. *Laser Techniques for Condensed-Phase and Biological Systems* 3273:115–133.

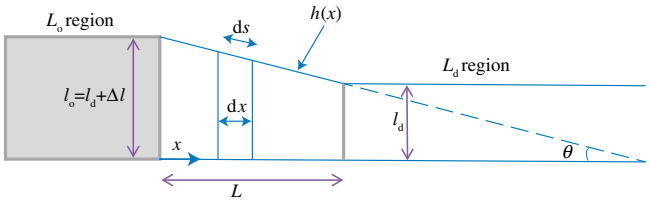

Fig. S1. Schematic of domain boundary in lipid monolayer structure

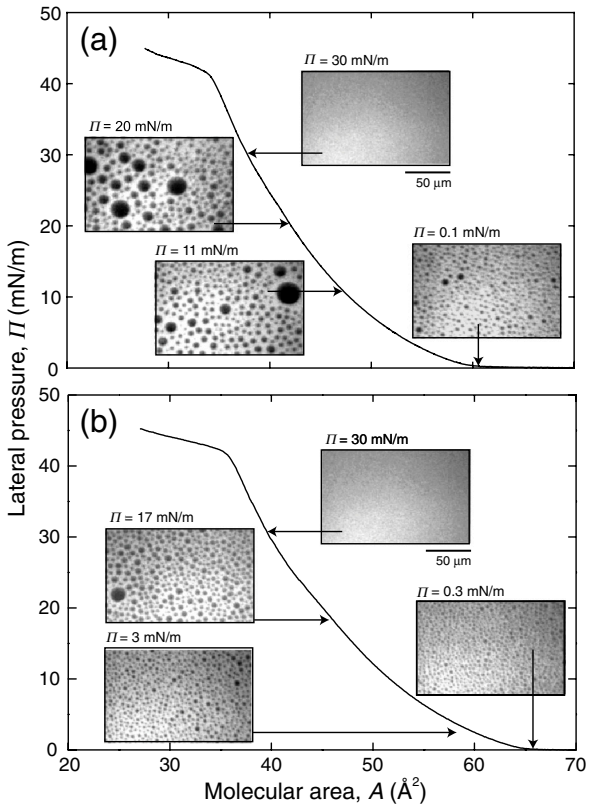

Fig. S2. Pressure-area (Π-*A*) isotherms and fluorescence images of (*A*) control and (*B*) EAE CYT myelin monolayers containing 1 wt% TR-DHPE on a MOPS buffer subphase at $T \approx 22$ °C and pH ≈ 7.2.

Table S1. Calculated λ with different parameters for hydrocarbon-air surface tension of $\gamma = 30$ mN/m

l_d (nm)	Δl (nm)	$\theta \approx 180(\Delta l/l_d)^{1/2}/\pi$	$\lambda_{min} \approx 0.08\gamma\Delta l(\Delta l/l_d)^{3/2}$ (fN)
1	0.1	18.1	7.6
2	0.1	12.8	2.7
2	0.3	22.2	42
2.5	0.1	11.5	1.9